AGU PUBLICATIONS

JGR

Journal of Geophysical Research: Oceans

RESEARCH ARTICLE

10.1002/2015JC011504

Key Points:

- Antarctic sea ice can be divided in four characteristic surface melt patterns
- Diurnal freeze-thaw cycles dominate the Antarctic summer melt
- Snowmelt on Antarctic sea ice does not show a significant trend in the last decades

Correspondence to:
S. Arndt,
stefanie.arndt@awi.de

Citation:
Arndt, S., S. Willmes, W. Dierking, and M. Nicolaus (2016), Timing and regional patterns of snowmelt on Antarctic sea ice from passive microwave satellite observations, *J. Geophys. Res. Oceans*, *121*, doi:10.1002/2015JC011504.

Received 25 NOV 2015
Accepted 12 JUL 2016
Accepted article online 14 JUL 2016

Timing and regional patterns of snowmelt on Antarctic sea ice from passive microwave satellite observations

Stefanie Arndt[1], Sascha Willmes[2], Wolfgang Dierking[1], and Marcel Nicolaus[1]

[1]Alfred-Wegener-Institut Helmholtz-Zentrum für Polar- und Meeresforschung, Bremerhaven, Germany, [2]Department of Environmental Meteorology, University of Trier, Trier, Germany

Abstract An improved understanding of the temporal variability and the spatial distribution of snowmelt on Antarctic sea ice is crucial to better quantify atmosphere-ice-ocean interactions, in particular sea-ice mass and energy budgets. It is therefore important to understand the mechanisms that drive snowmelt, both at different times of the year and in different regions around Antarctica. In this study, we combine diurnal brightness temperature differences (dT_B(37 GHz)) and ratios (T_B(19 GHz)/T_B(37 GHz)) to detect and classify snowmelt processes. We distinguish temporary snowmelt from continuous snowmelt to characterize dominant melt patterns for different Antarctic sea-ice regions from 1988/1989 to 2014/2015. Our results indicate four characteristic melt types. On average, 38.9 $\pm$ 6.0% of all detected melt events are diurnal freeze-thaw cycles in the surface snow layer, characteristic of temporary melt (Type A). Less than 2% reveal immediate continuous snowmelt throughout the snowpack, i.e., strong melt over a period of several days (Type B). In 11.7 $\pm$ 4.0%, Type A and B take place consecutively (Type C), and for 47.8 $\pm$ 6.8% no surface melt is observed at all (Type D). Continuous snowmelt is primarily observed in the outflow of the Weddell Gyre and in the northern Ross Sea, usually 17 days after the onset of temporary melt. Comparisons with Snow Buoy data suggest that also the onset of continuous snowmelt does not translate into changes in snow depth for a longer period but might rather affect the internal stratigraphy and density structure of the snowpack. Considering the entire data set, the timing of snowmelt processes does not show significant temporal trends.

1. Introduction

The energy fluxes through sea ice and its snow cover differ strongly between melting and freezing seasons [*Arndt and Nicolaus*, 2014; *Perovich and Polashenski*, 2012; *Perovich et al.*, 2002]. As Antarctic sea ice is covered with snow during most of the year [*Massom et al.*, 2001], transitions between these seasons strongly affect snow-property and snow-volume changes. Snow metamorphism and an increasing liquid water content in the snow pack at the spring-to-summer transition modify the surface energy budget by decreasing the surface albedo, causing increased absorption and transmission of solar radiation [*Brandt et al.*, 2005; *Massom et al.*, 2001]. Surface and subsurface snowmelt processes initiate melt water penetration through the snowpack and the subsequent formation of superimposed ice at the snow-ice interface [*Brandt and Warren*, 1993; *Haas*, 2001]. Moreover, it results in a decreasing snow depth. Internal snowmelt contributes to the sea-ice mass balance of Antarctic sea ice [*Eicken et al.*, 1994; *Haas et al.*, 2001; *Massom et al.*, 2001].

Passive microwave sensors can detect changes of the snow liquid water content as it leads to a substantial alteration of the microwave emissivity ε and hence of brightness temperature T_B [e.g., *Foster et al.*, 1984; *Ulaby et al.*, 1986]. The seasonal evolution of snowmelt and the associated changes in T_B differ significantly between the Arctic and the Antarctic [*Andreas and Ackley*, 1982; *Nicolaus et al.*, 2006; *Willmes et al.*, 2014]. On Arctic sea ice, the formation of liquid water during initial surface melt leads to increasing ε and T_B [*Comiso*, 1983; *Drobot and Anderson*, 2001]. As soon as slush and/or melt water forms at the ice surface, T_B decreases again due to the high free-water content [*Garrity*, 1992]. The subsequent widespread ponding is triggered by air temperatures remaining consistently above the freezing point [e.g., *Flocco et al.*, 2012; *Nicolaus et al.*, 2010; *Rösel and Kaleschke*, 2012; *Webster et al.*, 2015]. Based on the distinct seasonal cycle of microwave signatures of Arctic sea ice, *Belchansky et al.* [2004]; *Livingstone et al.* [1987]; and *Markus et al.* [2009] identified different stages of melt transition.

In contrast, snow on Antarctic sea ice generally persists year-round, but undergoes substantial seasonal changes in physical properties [*Massom et al*., 2001]. The transport of cold, dry air masses from the continental shelf leads to a low relative humidity and weak surface snowmelt during austral spring [*Andreas and Ackley*, 1982]. Instead, *Eppler et al*. [1992] and *Willmes et al*. [2006, 2009] describe diurnal thawing and refreezing of snow as measured by variations of surface microwave properties, which can be used to identify the onset of surface melt. The diurnal freeze-thaw cycles cause widespread layers of metamorphous snow with increased snow grain sizes, dense layers and superimposed ice, which forms at the snow-ice interface on Antarctic sea ice [*Nicolaus et al*., 2009].

Willmes et al. [2009] detected the snowmelt onset on Antarctic sea ice using differences in microwave brightness temperatures at 37 GHz, measured in the morning and evening, using a fixed threshold. However, the depth, at which diurnal freeze-thaw cycles are effective in the snow, differs regionally and temporally due to varying snow properties and atmospheric conditions. Hence, also snow layers below the penetration depth of the 37 GHz channel need to be monitored. We therefore investigate the additional use of the 19 GHz channel which provides more detailed information on the stage of subsurface melt processes because of the larger penetration of longer microwaves into the snowpack [*Abdalati and Steffen*, 1997; *Ashcraft and Long*, 2003].

The aim of this study is to determine the timing of snow melt onset, to distinguish dominant surface melt processes, i.e., temporary and continuous melt, and to analyze their regional characteristics. To do this, we use locally determined thresholds for the identification of freeze-thaw cycles, and include an additional microwave parameter that is considered indicative of strong and continuous melt. We analyze microwave brightness temperature time series from 1988/1989 to 2014/2015, to study the long-term variability in snowmelt processes and their spatial distribution. These spatio-temporal characteristics of snowmelt on Antarctic sea ice can contribute to a better understanding of the uncertainty and variability of sea-ice concentration and snow-depth retrievals in regions of high sea-ice concentrations [*Andersen et al*., 2007; *Markus et al*., 2006; *Comiso and Kwok*, 1996].

2. Melt Transition Retrieval From Passive Microwave Data

2.1. Background

The seasonal variability in the physical properties of snow has strong effects on its microwave properties. The microwave emissivity ε of snow and the measured microwave brightness temperature T_B are functions of frequency f and polarization p. They are related by

$$T_B(f,p) = \varepsilon(f,p) \cdot T_S, \tag{1}$$

where T_S is the effective physical temperature of the emitting body [*Ulaby et al*., 1986].

Dry snow appears almost transparent to microwave frequencies below approximately 30 GHz, which means that the measured T_B is mainly influenced by the upper ice layer. Signals acquired at higher frequencies have lower penetration depths and are therefore partly or entirely influenced by the snow properties, even when the snow is dry (the penetration depth into dry snow at 37 GHz is about 0.5 m [*Garrity*, 1992]). When snow starts to melt, surface scattering increases and volume scattering decreases [*Mätzler and Hüppi*, 1989]. As the liquid water content of the snowpack increases, the water absorbs more microwave energy, which causes the snowpack's microwave emissivity to increase [*Abdalati and Steffen*, 1997; *Tedesco*, 2015]. *Abdalati and Steffen* [1995] show that the associated T_B increase is more pronounced at horizontal than at vertical polarization. This polarization difference diminishes with increasing snow wetness due to changes in dielectric properties at the air-snow interface. Moist snow affects the brightness temperature at all frequencies as well as its penetration depth. For liquid water contents larger than 2%, *Ulaby et al*. [1986] determined a reduction in penetration depth to about 2 cm at 37 GHz, and to 8 cm at 19 GHz.

Comparing surface melt processes of Arctic and Antarctic sea ice, significant differences are obvious between both hemispheres [*Nicolaus et al*., 2006]. In contrast to the Arctic, no persistent and large-scale formation of liquid water in the snowpack occurs in the Antarctic [*Drinkwater and Liu*, 2000]. As soon as the spring-summer transition starts, the snow surface melts during the daytime (causing higher values of T_B) and refreezes during the nighttime (causing a decrease of T_B). Consequently, *Willmes et al*. [2009] relate the

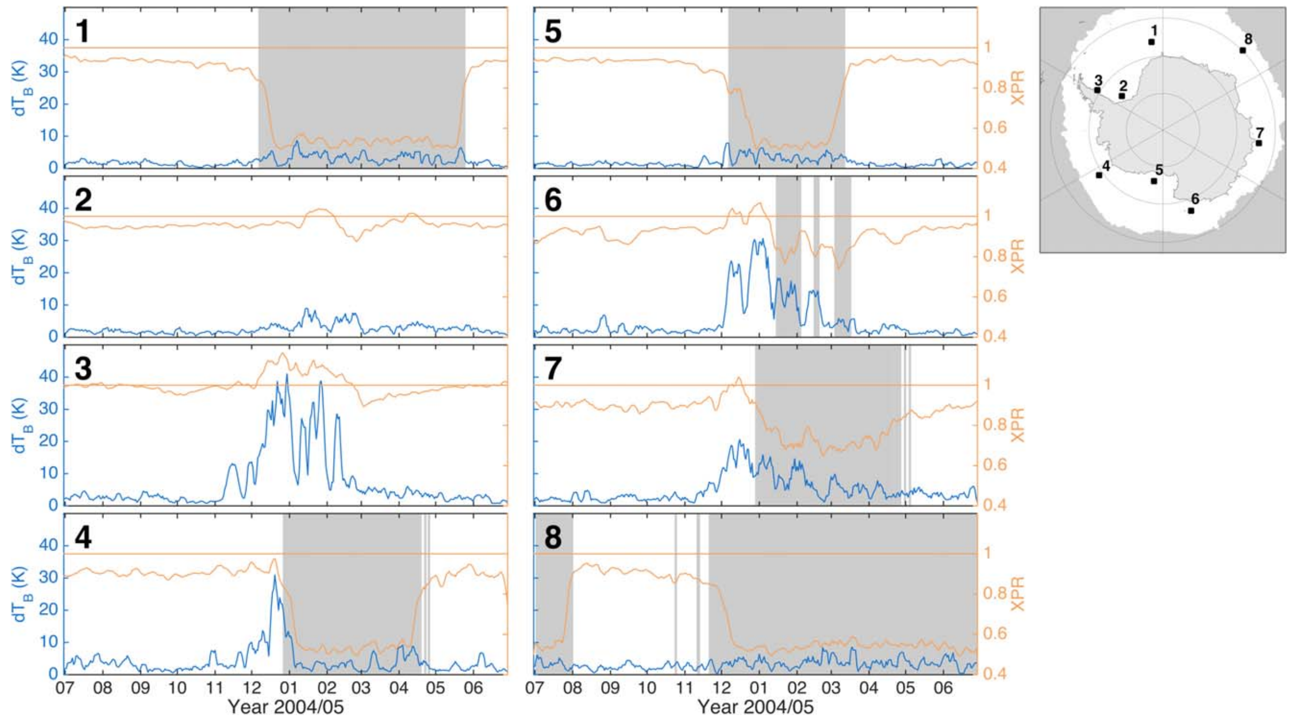

Figure 1. Example time series of diurnal variations in brightness temperature (dT_B, blue) and the cross-polarized ratio (XPR, orange) for 8 locations in the Antarctic sea-ice area (top right plot), July 2004 to June 2005. Grey-shaded areas indicate a sea-ice concentration below 70%. In the top right map, the white areas indicate the maximal sea-ice covered area of the previous year.

observed diurnal brightness temperature differences to temporary thawing and refreezing of snow. Due to the frequent diurnal freeze-thaw cycles, snow grain sizes increase, and extensive snow metamorphism begins. This metamorphism decreases the microwave emissivity and thus T_B, in contrast to the increase of these parameters for Arctic sea ice since the liquid water content increases drastically as soon as surface melt starts [*Markus et al*., 2009].

2.2. Melt Onset Proxies From Passive Microwave Data

2.2.1. Diurnal Variation of Brightness Temperature (dT_B)

Willmes et al. [2006] identified the onset of summer melt on Antarctic sea ice by combining passive-microwave observations and field measurements during the Ice Station POLarstern expedition (ISPOL, summer 2004/2005 [*Hellmer et al*., 2006]). By analyzing time series of the absolute difference between the two diurnal T_B values from ascending and descending satellite passes (dT_B, 37 GHz, vertically polarized) they found an increase of dT_B once the temporary snowmelt onset at the snow surface started. Their algorithm defines the onset of summer conditions typical for the Weddell Sea as the first date at which the dT_B exceeds a fixed threshold of 10 K for at least 3 consecutive days.

Here we show that the characteristics of the seasonal dT_B evolution (blue curves in Figure 1) differ mainly in (1) timing and magnitude of the absolute maximum of the dT_B values (in the following denoted as *peak value*), and (2) the length of the period with increased dT_B values as compared to the pre-summer season (the period with the highest peaks, here denoted as *peak broadness*). E.g., Location 7 indicates a peak value of 26.0 K, whereas dT_B rises up to 41.1 K at Location 3. Furthermore, the peak broadness differs from 1 month, e.g., at Location 4, in areas of dropping sea-ice concentration (SIC), up to 4 months, in all-year ice-covered areas such as Location 3. These regional differences in the peak value and peak broadness of the summer dT_B evolution will be considered in our approach of snowmelt onset detection by locally determined thresholds of dT_B.

2.2.2. Cross-Polarized Ratio XPR

Combining T_B at different frequencies and polarizations allows distinguishing different stages of the melt progress. *Ashcraft and Long* [2003] introduced ratios of T_B from various SSM/I channels to characterize surface and subsurface melt. The use of ratios has the advantage of reducing the effects of physical

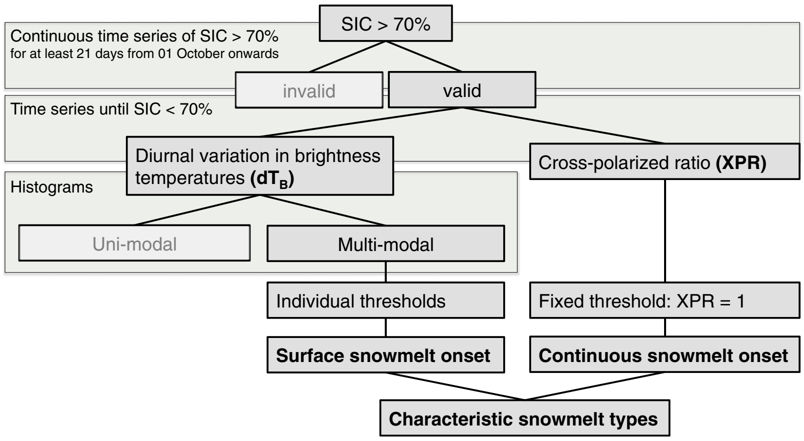

Figure 2. Flowchart of the snowmelt onset retrieval algorithm based on sea-ice concentration (SIC) and brightness temperature (T_B) data.

temperature changes. Their analyses reveal that the combination of the horizontally polarized brightness temperature at 19 GHz (T_B(19H)) and the vertically polarized brightness temperature at 37 GHz (T_B(37V)) is most sensitive to both surface and subsurface melt. In the context of the present paper this ratio is introduced as the cross-polarized ratio XPR:

$$XPR = T_B(19H) \cdot T_B(37V)^{-1}. \tag{2}$$

When melt water drains from the upper snowpack to deeper layers, the emissivity of the 19H channel increases and even exceeds the emissivity of the 37V channel [*Abdalati and Steffen*, 1997]. Hence, the XPR can be used as indicator for snow soaked from above by melting water. Even though the studies by *Abdalati and Steffen* [1997]; and *Ashcraft and Long* [2003] were performed on Greenland ice sheets, the microwave response to changes in surface snow properties can be assumed to be comparable to snow on (Antarctic) sea ice. However, for sea ice, one needs also to take into account a possible flooding of the snow-ice interface (e. g. in case of too heavy snow load) that influences the measured XPR value (see section 4.1), and in some cases the influence of the sea ice below.

In Figure 1 two different regimes of XPR (orange curves) can be separated. One regime (locations 1, 4, 5, and 8) is characterized by XPR values less than 0.95 throughout the year indicating significant drops and rises with decreasing and increasing SIC. The second regime (locations 2, 3, 6, and 7) shows larger variations and XPR values that eventually exceed 1 between December and January. For Locations 3, 6, and 7 this XPR increase seems to be associated with an increasing dT_B. For Location 3, XPR exceeding 1 just occurs shortly before the strong increase of dT_B. In contrast, Location 2 reveals a sharp increase in XPR mid of January without preceding strong diurnal freeze-thaw cycles.

If the detected XPR values are above 1, the emissivity at 19H is larger than at 37V. We associate this with melt water draining into the lower snowpack and define a threshold of XPR=1 as an indicator for the onset of continuous snowmelt on Antarctic sea ice.

Even though strong and continuous melt is rarely observed as stated by *Willmes et al*. [2009], we intend to use this parameter here to complement our observations of freeze-thaw cycles by identifying regions where continuous melt does in fact occur. Compared to the diurnal freeze-thaw cycles that mainly influence physical snow properties at the surface and thus, e.g., alter the amount of reflected and absorbed radiation (energy budget), the continuous snow melt might cause a loss in snow volume related to changes in the mass budget of the snowpack.

2.3. Melt Transition Retrieval

Figure 2 outlines the methodology to derive the timing of snowmelt onset with a regionally adaptive approach. We minimize the effects of open water on the T_B signal by including only grid cells where SIC is equal or larger than 70% for at least three weeks from 1 October onward. The following analysis is applied for every grid cell until the sea-ice concentration drops once below 70%. In a next step, a 5 day running

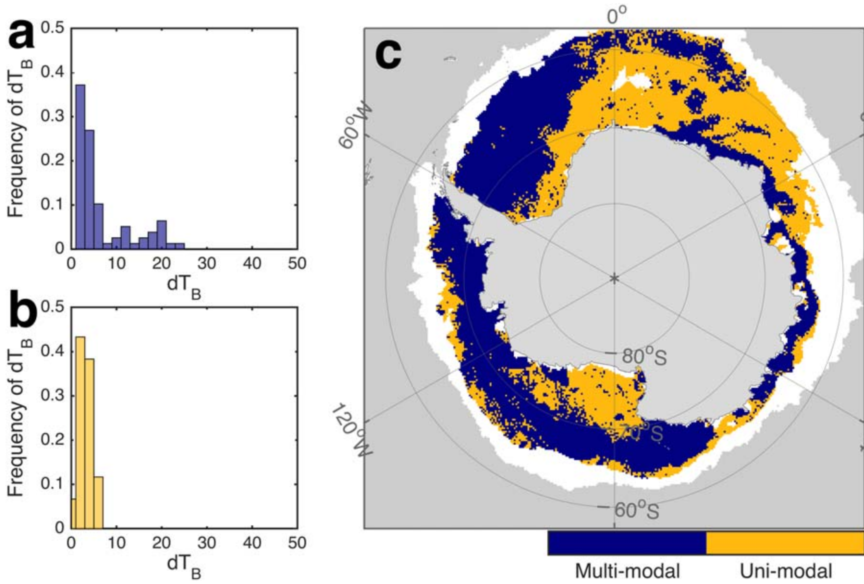

Figure 3. One example grid cell of (a) multimodal and (b) uni-modal distribution of dT_B and (c) its spatial distribution for the example melt season 2004/2005. The histograms contain only values for sea-ice concentrations>70% from 1 October to 31 January. The white areas indicate the maximum sea-ice area of the previous winter.

mean is applied to each grid-cell T_B time series. From the T_B data obtained at 37V, we calculate dT_B and derive its histogram for each grid cell (bin width 2 K) over the expected melting season. An example is shown in Figures 3a and 3b. The derived histograms can be subdivided into uni-modal and multimodal distributions. We define a mode as a local maximum bounded by at least one lower bin on each side. A multimodal distribution has to reveal at least two of these modes. If a mode exceeds a proportion of 90% of all included data points, the distribution is defined as uni-modal. The multimodal distributions (Figures 3a and 3c; blue) reflect the different melt stages of snow and the associated differences in freeze-thaw cycle strengths. Data points with a uni-modal distribution, and thus predominantly low dT_B values (Figures 3b and 3c; orange) are neglected in the analysis of diurnal freeze-thaw cycles, as they do not reveal the characteristic diurnal surface variations. In the next step, we define the individual dT_B-threshold criterion for the detection of temporary snowmelt applying an iterative threshold selection algorithm [*Ridler and Calvard*, 1978] to the pixels with multimodal dT_B distribution. Finally, the *Temporary Snowmelt Onset* (TeSMO) is defined as the first time when dT_B exceeds the respective local threshold for at least 3 consecutive days during the expected melting season from 1 October to 31 January (e.g., Figure 4b).

The *Continuous Snowmelt Onset* (SMO) is detected independent of the previous described Temporary Snowmelt Onset. For its retrieval we apply the same SIC constraint as for the TeSMO (compare Figure 2). Again, a 5 day running mean is applied to each XPR time series, respectively, to reduce the effect of noise and outliers. Subsequently, SMO can be determined in areas with an XPR exceeding 1 for at least 3 consecutive days. The first of the 3 days is interpreted as the day of melt onset. In case, we observe an earlier SMO than TeSMO, we neglect the later as we interpret it as a premelt stage of SMO (e.g., Location 3, Figure 1).

2.4. Data Sets

Our analysis is based on the Level-3 Equal-Area Scalable Earth-Grid (EASE-Grid) Brightness Temperature data set, provided by the US National Snow and Ice Center (NSIDC) [*Armstrong et al*., 1994]. Daily brightness temperatures (T_B) at vertical and horizontal polarization are derived for July 1987 to June 2015 for 4 channels (19 GHz, 22 GHz, 37 GHz, and 85 GHz) from ascending and descending orbits on a 25 km grid. In our study we employed the 19 GHz- and 37 GHz-channels as explained above. During this period, data of four different SSM/I sensors were used: F8 from July 1987 to December 1991, F11 from December 1991 to 1995, F13 from May 1995 to December 2008, and F17 from December 2006 onward. *Willmes et al*. [2009] specified the differences in dT_B during the overlap periods to be negligible. The reason is that dT_B represents a 12 h variation of measured raw brightness temperatures and is therefore less sensitive to small inter-sensor

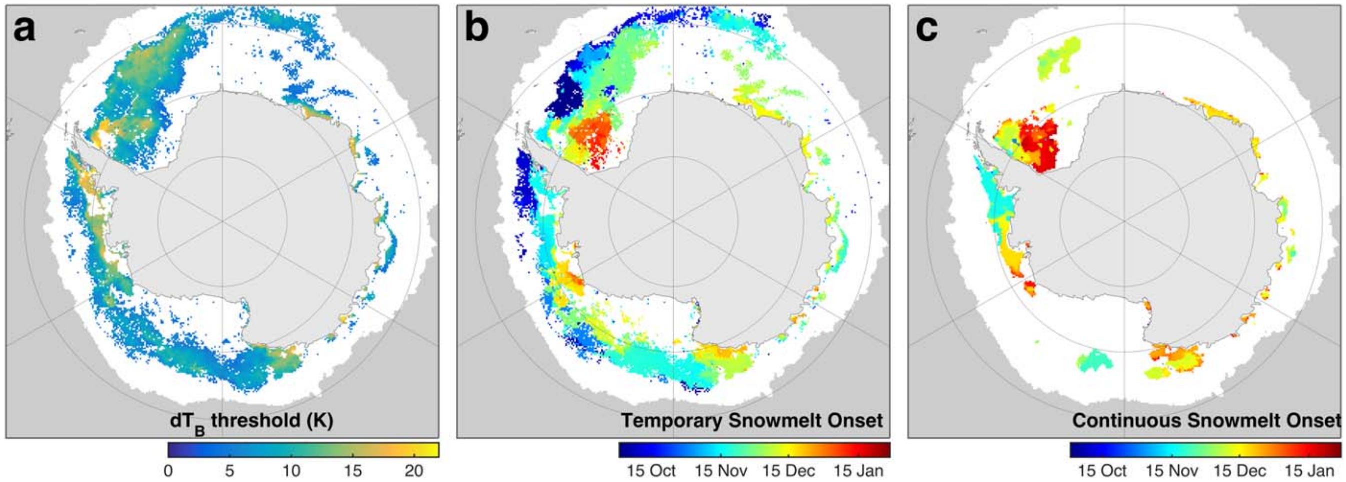

Figure 4. (a) Individual transition threshold dT_B, (b) Temporary Snowmelt Onset, and (c) Continuous Snowmelt Onset for the melt transition 2004/2005. The white areas indicate the maximal sea-ice-covered area of the previous winter.

differences between the ascending and descending nodes. All daily brightness temperature data are interpolated to a 25 km SSM/I polar stereographic grid, using nearest-neighbor resampling.

Bootstrap sea-ice concentration (SIC) data from Nimbus-7 SMMR and DMSP SSM/I-SSMIS Passive Microwave Data product were used to define the areas with SIC $>$ 70% for which the algorithm is valid (section 2.3) [*Comiso*, 2004]. The data are available daily from late 1978 to 2014 on a 25 km SSM/I polar stereographic grid. During this period, the same four different SSM/I sensors were as for the brightness temperature data set (F8, F11, F13, F17) and can be used without any further inter-sensor adjustment [*Comiso and Nishio*, 2008]. The time period from January 2015 onward is covered by the near-real-time DMSP SSMIS Daily Polar Gridded Sea Ice Concentration data product [*Maslanik and Stroeve*, 1999].

3. Results

3.1. Spatial Variability of Snowmelt Patterns

Figure 4 shows the obtained individual dT_B transition thresholds (Figure 4a) and the associated Temporary Snowmelt Onset (TeSMO, Figure 4b) as well as the Continuous Snowmelt Onset (SMO, Figure 4c) for the melt season 2004/2005, respectively. The example year of 2004/2005 was chosen to ensure the best possible comparison with the previous study by *Willmes et al*. [2009]. The white areas cover the previous winter's maximum sea-ice extent, and indicate locations that do not fulfill the requirements for melt-onset detection (section 2.3). For the following description and analysis, we divided the Antarctic sea-ice area in five areas: Indian Ocean (20°E to 90°E), Western Pacific Ocean (90°E to 160°E), Ross Sea (160°E to 130°W), Bellingshausen and Amundsen Seas (130°W to 60°W), and Weddell Sea (60°W to 20°E) [*Gloersen et al*., 1992].

The individual transition thresholds dT_B cover a range from 3 to 22 K with a modal value of 6 K and a mean of 8.9 $\pm$ 3.6 K for the melt season 2004/2005. The distribution of dT_B thresholds shows substantial spatial variability. The Ross Sea tends to have lowest thresholds, between 3 and 10 K, indicating least pronounced melt-freeze cycles. Also parts of the eastern Weddell Sea and pack ice area in the Indian Ocean reveal low dT_B values. In contrast, the highest transition thresholds (up to 22 K) are found in the Amundsen and Weddell Seas. In addition, high dT_B values are common for most of the land-fast sea ice on the coast of East Antarctica.

Based on these individual thresholds, the derived TeSMO shows a latitudinal dependence, with an earlier melt onset in the marginal sea-ice zone, and melt spreading southward as the summer progresses. During the melt season 2004/2005, the average TeSMO for the entire Antarctic occurred on 20 November, ranging from 10 November in the Bellingshausen and Amundsen Seas to 05 December in the Western Pacific Ocean. The latest TeSMOs occurred in the southwestern Weddell Sea and at the coast of the eastern Ross Sea in the beginning of January.

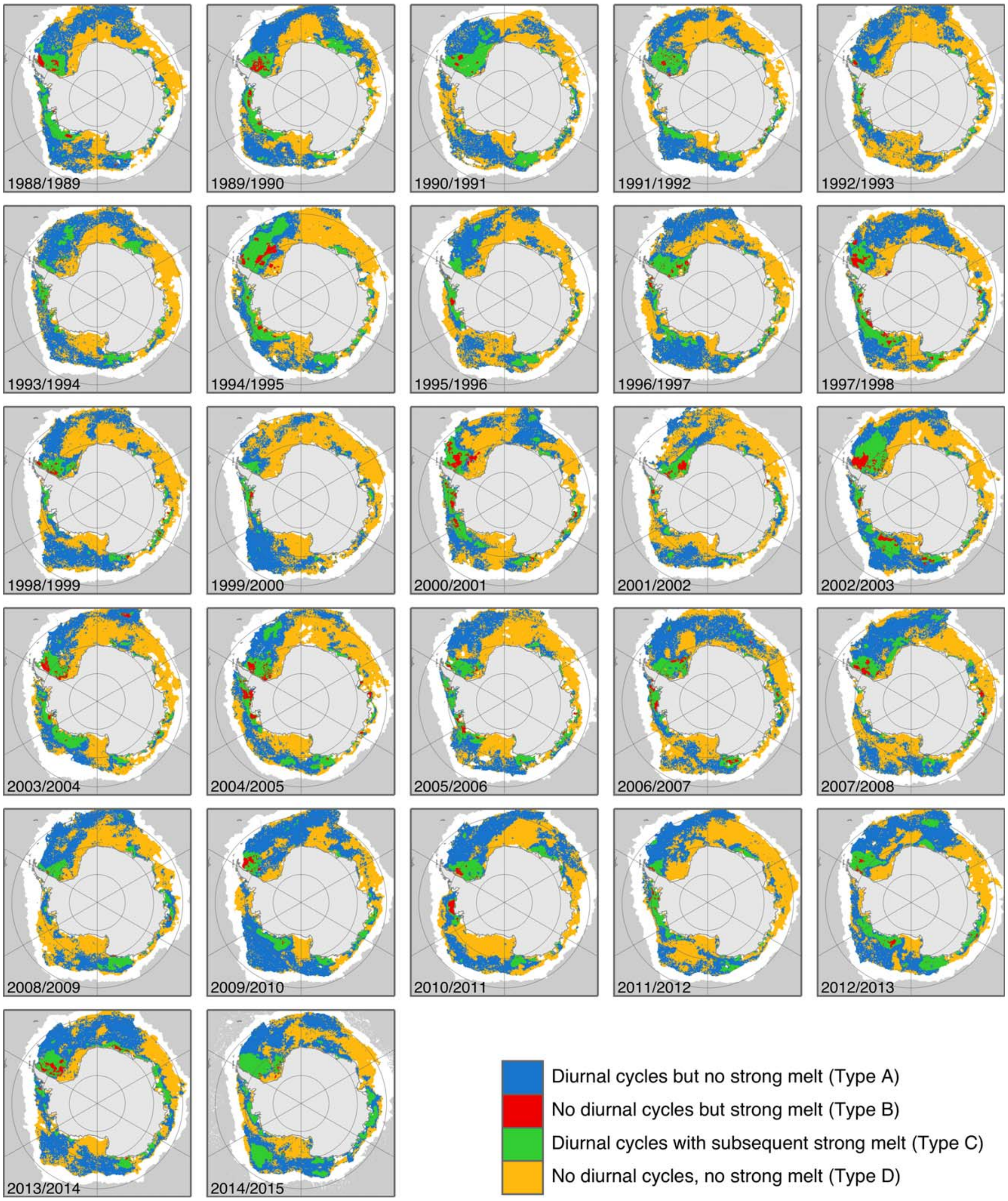

Figure 5. Classification of Antarctic sea ice into four characteristic snowmelt types for the seasons from 1988/1989 to 2014/2015. The white color represent unclassified zones, and indicates the maximal sea-ice-covered area of the previous winter.

The latitudinal dependence of SMO is difficult to analyze because of the relatively small areas affected by this type of melt. The regional dependence might be connected to local weather phenomena as well as peculiarities in snow and ice properties. During the melt season 2004/2005, SMO occurred, on average, 17 days later than TeSMO, in an interval from 30 November (Bellingshausen and Amundsen Seas) to 23 December (Weddell Sea). Spatial variations in the derived local thresholds and retrieved melt onset dates are discussed in section 4.1.

3.2. Characteristic Regions and Surface Melt Types

To link the two stages of snowmelt onset described above with different snow surface characteristics of Antarctic sea ice, we distinguish four ice zones based on their typical melt signatures (Figure 5): diurnal freeze-thaw cycles in the surface snow layer only (Type A), immediate continuous snowmelt throughout the snowpack (Type B), diurnal surface freeze-thaw cycles followed by continuous melt (Type C), and no observed melt at all (Type D). A fifth category is marked as "not classified" (Figure 5, white areas). The results are shown for each year of the available time series from 1988/1989 to 2014/2015.

On average, about 12% of the classified sea-ice area reveals diurnal freeze-thaw cycles with subsequent continuous melt (Figure 5, Type C: green). This surface type prevails in the western Weddell Sea, the eastern West Pacific sector, and on the land-fast sea ice in the East Antarctic. It is characterized by freeze-thaw cycles at the surface resulting in melt water penetration to deeper layers, which eventually soaks the entire snowpack

Areas with freeze-thaw cycles starting early in the season, but without a subsequent detection of continuous melt, are observed in the outflow area of the Weddell Gyre in the northern Weddell Sea, as well as in the northern Amundsen and Ross Seas (Figure 5, Type A: blue). This surface type usually has early and weak surface melt and dominates the Antarctic sea-ice area covering about 39% of the classified sea-ice area.

Unlike the two latter surface types, where we observe at least short periods of characteristic freeze-thaw cycles during summer, small areas of the Antarctic sea ice (less than 2%) reveal continuous melt with no refreezing events (Figure 5, Type B: red) or delayed increase in freeze-thaw cycles compared to the continuous (deep) melt onset (Figure 1, Location 3).

Major parts of the Indian and Western Pacific Oceans, as well as the southeastern Weddell Sea and central Ross Sea (in total 48% of the classified sea-ice area), reveal neither diurnal freeze-thaw cycles at the snow surface nor continuous melt (Figure 5, Type D: yellow). Some of these sea-ice regions may already disintegrate by break-up or lateral and bottom melt, before significant surface melt can take place. In others of these regions, our detection criteria may not be sufficiently sensitive to possible melt onset.

The eastern Weddell Sea is dominated by the predominant clockwise sea-ice drift related to the Weddell Gyre [*Schmitt et al.*, 2004] and the interaction with the adjacent Filchner Trough [*Nicholls et al.*, 2009]. The southern Ross Sea is most commonly affected by katabatic winds from the shelf ice leading to the formation of the coastal Ross Sea Polynya. These interactions between ocean, sea ice and atmosphere lead for both the Weddell and Ross Sea to a repeated formation of new thin ice [*Smith et al.*, 1990]. Consequently, these areas of newly formed ice are snow-free, or are covered only by a thin snow layer. Thus, the received microwave signal is dominated by the sea-ice surface and its characteristics. Also the highly dynamic ice conditions due to the sea-ice production in these regions prevent the detection of melt based on dT_b and XPR.

The surface and snow layer properties of large areas of pack ice in the Indian and Western Pacific Oceans are affected by a highly dynamic ice regime and the thin snowpack (less than 20 cm [*Worby et al.*, 2008]). The marginal ice zone is dominated by formation of ice and the penetration of ocean waves into the ice. Snow layers are thin and may get wet due to potential flooding caused by the penetrating ocean waves. In some cases, the snow may be heavy enough to lower the ice surface below water level. Hence, also in this case, the use of dT_b and XPR is not suitable for the detection of melt onset (see Type D). In addition, the marginal ice zone is influenced by the Antarctic Circumpolar Current, which causes continuous sea-ice divergence and disintegration, resulting in enhanced bottom and lateral melt in the area once the cooling from the atmosphere has finished.

4. Discussion

4.1. Limitations and Uncertainties

The spatial homogeneity of melt patterns is derived from the standard deviation of a grid cell and its eight neighbors (i.e., in an overlapping window of 3 x 3 cells) for the data products dT_B threshold, TeSMO, and

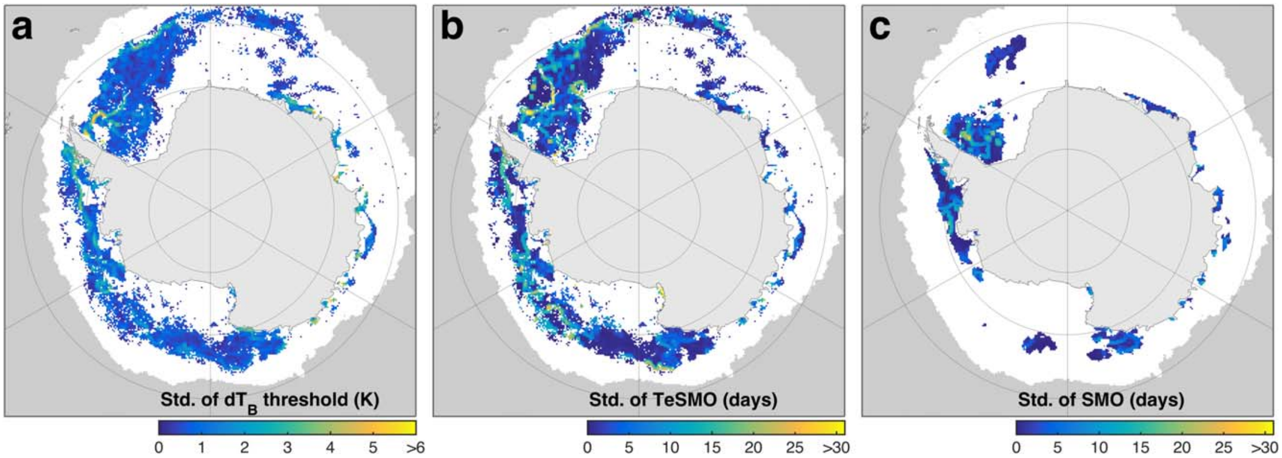

Figure 6. Derived standard deviations (Std.) derived from overlapping windows of 3 × 3 cells for (a) the individual transition threshold dT_B, (b) the Temporary Snowmelt Onset (TeSMO), and (c) the Continuous Snowmelt Onset (SMO) for the melt transition 2004/2005. The white areas indicate the maximal sea-ice-covered area of the previous winter.

SMO (see Figure 6). This approach gives a measure for local signature variations in an area of 75-by-75 km. As possible reasons for variations, we consider also small-scale snowdrift and sea-ice drift in addition to different snow properties and ice conditions (e.g., sea-ice age classes). The influence of sea-ice drift is not included in our approach, since no adequate data products are existent. However, if these data would be available, we expect improvements primarily in the marginal ice zones and less for the inner pack ice.

For the example year of 2004/2005, the mean variation of TeSMO over the 3 x 3 grid cell boxes is 4.5 days, with 69% of all variations smaller or equal to 5 days and a modal value of 1 day (Figure 6b). The respective dT_B threshold reveals a mean spatial variation of 0.9 K (Figure 6a) whereas the modal value is between 0.5 and 0.6 K. The highest variations in TeSMO and dT_B (up to 30 days/6.3 K) are found between zones of different melt regimes in the Weddell Sea (Figures 4 and 5). Spatial variations of SMO show a mean of 3.6 days, with 52% of all derived variations smaller or equal to 2 days (Figure 6c).

The more heterogeneous distribution of TeSMO compared to SMO may be linked with the sensitivity of both parameters to snow depths: Because of the smaller penetration depth of the 37 GHz channel, the retrieval of TeSMO is more strongly affected by localized processes on the snow surface, such as for instance snow drift, whereas SMO, which is derived from the XPR including the 19 GHz brightness temperature, is influenced by the deeper snow layers, where continuous snowmelt is mainly triggered by solar radiation and related cloud effects (i.e., changes in long-wave radiation) which is spatially less variable than, e. g., snow drift patterns on the surface.

We assume that the observed TeSMO and SMO patterns indicate the influence of a number of different snow and ice parameters (e.g., sea-ice/snow age), and processes. The sea-ice concentration range that we accept for our retrievals varies between 70% and 100%. Due to the ice drift, the distribution of open water and sea ice in a given area changes within hours to days. The drift causes also a redistribution of snow zones with different properties (e. g. depth). In addition we have to consider the uncertainties in the retrieval of the melt onset (see below).

An overall quantification of uncertainties of the presented method is not possible, since measurements providing daily air temperatures close to the snow/ice surface are not available. Since our method requires that dT_B and XPR exceed their respective threshold for at least 3 consecutive days, we might miss shorter melt events actually taking place earlier. This discrepancy may account for several days in the worst case.

Moreover, the brightness temperature and the retrieved melt onset data may be biased due to the presence of open water areas. Table 1 gives an overview about the influence of the chosen threshold in sea-ice concentration on the retrieved TeSMO and SMO. Since open water blurs the microwave signal and thus, e.g., diminishes the diurnal variations at the snow surface, the defined melt criteria are fulfilled slightly later in areas of less sea-ice concentration. Thus, we can conclude from this sensitivity study that areas of sea-ice concentration close to 70% may be biased toward a later melt onset, whereas in completely ice-covered

Table 1. Sensitivity Study on Different Sea-Ice Concentration Thresholds for the Retrieval Temporary Snowmelt Onset (TeSMO) and Continuous Snowmelt Onset (SMO) for the Melt Transition 2004/2005

	TeSMO/SMO (Days After 1 Oct)				
Sea-ice concentration >	50%	60%	70%	80%	90%
Indian Ocean	52/78	51/77	51/76	51/75	50/75
Western Pacific Ocean	71/81	71/80	71/79	71/77	70/76
Ross Sea	49/70	49/69	48/68	48/67	46/63
Bellingshausen and Amundsen Seas	42/63	42/62	41/61	39/59	36/56
Weddell Sea	61/84	61/84	60/84	60/84	58/84
All areas	56/76	56/76	54/75	54/75	52/75

[a]Numbers are given as the spatial mean for the respective region (days after 1 October). Calculations were only performed for grid cells, which are covered by the analysis for all five sea-ice concentration thresholds.

areas an earlier melt onset can be expected. Overall, the Bellingshausen and Amundsen Seas show the highest influence of the chosen sea-ice concentration threshold on the derived melt onset dates with a difference of up to 7 days in the presented study (Tab. 1), which might be connected to the comparable narrow and highly variable sea-ice band in the area. Taken the entire Antarctic sea-ice area into account, the influence is rather small since TeSMO and SMO vary by 1 and 4 day(s), respectively.

Another limiting factor of the presented study is flooding of Antarctic sea ice. In our retrieval of melt onset, we do not consider situations in which a relatively thick snow cover on relatively thin ice may lead to a negative freeboard and thus, to flooding of the ice. While the bottom snow layer is soaked with water, the snow surface, and thus the detection of temporary snowmelt, may still be unaffected. Nevertheless, as the penetration depth of microwave signals at 37 GHz is up to 50 cm for dry snow [*Garrity*, 1992], the soaked bottom layer may lead to changes in the brightness temperatures, which would result in the retrieval of (continuous) snowmelt onset dates that are too early.

4.2. Comparisons of Surface Melt Patterns With Field Data and Previous Studies

4.2.1. Comparison With Autonomous Measuring Systems

A validation of the characteristic surface patterns (Figure 5) and their spatial variability (Figure 4) with field observations is almost impossible since field data with adequate spatial and temporal resolution and coverage are not available. Alternatively, comparisons with numerical simulations of snow cover properties could be performed, but currently no reliable simulations of snow properties and snow depth evolutions are available for the Weddell Sea. Here we compare data from autonomous Snow Buoys to assess our results at least for parts of the Weddell Sea during summer 2014/2015, when these data are available.

Snow Buoys (Met Ocean, Canada) are autonomous platforms deployed on sea ice. Four ultra sonic sensors measure the distance to the snow surface that is then transformed to snow depth. In addition, each buoy measures air temperature and surface pressure. Here we use data from four of these Snow Buoys: 2014S9, 2014S10, 2014S11, and 2014S12 *(hereafter only S9 to S12*, http://data.seaiceportal.de/*)*. The buoys were deployed in the southern Weddell Sea in January/February 2014, and obtained continuous and consistent measurements all through the austral summer 2014/2015. Figure 7a shows the drift trajectories of all four buoys, also indicating the regional spread of the measurements due to the individual drift trajectories. The black segments represent the drift path during the melt season 2014/2015, from October 2014 to January 2015. To our knowledge, this data set is the only one showing temporal changes of snow conditions over an entire summer, simultaneously for different locations in the Southern Ocean. Nearest-neighbor grid points of the daily buoy positions were extracted from our snowmelt data sets (TeSMO and SMO) for the following comparison. Snow depths from the buoys are given as a daily average of all four sensors of the respective buoy (Figure 7b).

Comparing all four buoys, differences between S10 and S12, located in the southeastern Weddell Sea during summer 2014/2015, and S09 and S11, drifting through the northwestern Weddell Sea during summer, become obvious. S9 and S11 stay in an area of temporary melt at the snow surface with subsequent continuous melt (Figure 7a, Type C, green), whereas the surrounding of buoy S12 is supposed to have neither temporary melt nor continuous deep melt (Type D, yellow). The surface characteristics in the surrounding sea-ice area of S10 are quite patchy and do therefore allow only for the determination

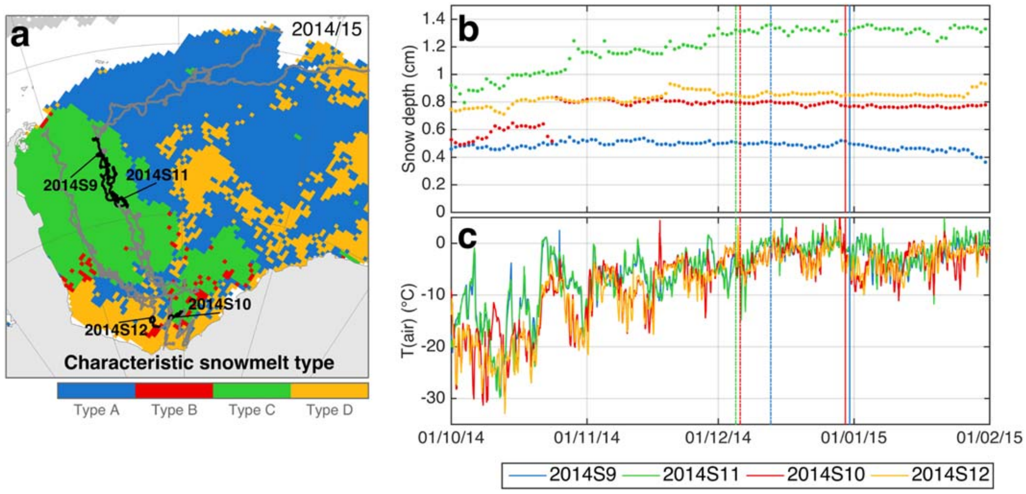

Figure 7. (a) Snow buoy tracks plotted on the characteristic snowmelt type for the melt transition 2014/2015. The black segments indicate the buoy drift during the expected melt season 2014/2015 (1 October 2014 to 31 January 2015), while the grey parts show the drift patterns during the freezing season. (b) Daily averaged snow depth, and (c) air temperature for all four buoys during the expected melt season 2014/2015. Dotted vertical lines indicate the extracted TeSMO, solid lines the extracted SMO for the respective buoys.

of temporary melt for the buoy from our analysis (05 December 2014, Figures 7b and 7c, dotted vertical line).

While the air temperatures of S9 and S11 exceed 0°C in the end of December as well as the end of January (Figure 7c), the snow depth measurements indicate no significant snow loss during the expected melt period (Figure 7b): The snow depth at S09 is stable around 0.5 m until the continuous snowmelt (SMO) is detected and it decreases by approximately 0.1 m, whereas snow depth at S11 increases until the beginning of temporary melt (TeSMO) and afterward varies around the seasonal maximum of 1.3 m. In contrast, S10 shows an increase until mid of October (mainly due to one strong snow fall event of 20 cm) and thereafter very stable snow conditions around 0.8 m, whereas S12 reveals a generally low variability in snow depth over the entire melt period between 0.7 and 0.9 m.

Generally, air temperatures above the freezing point become more dominant after the detected temporary melt onsets for the respective buoys. The apparent change between thawing (temperatures above the freezing point) and refreezing (temperatures below the freezing points) is the main characteristic of the described temporary melt.

Considering both, the characteristic snowmelt type and the time series of snow depth and air temperature for all four buoys, we notice that also continuous (deep) snowmelt is not necessarily associated with an immediate decreasing snow depth. In the vicinity of buoy S9 and S11, we expect perennial sea ice [*Nghiem et al*., 2016] and thus a multiyear snowpack on top. The latter is characterized by layers of highly compacted and metamorphic snow with internal ice layers [*Nicolaus et al*., 2009]. If the described continuous melt onsets and thus the liquid water content in the deeper snowpack increases, the compacted layers of the multiyear snowpack are stable enough to prevent a drop in snow depth. Thus, changing physical properties of snow on Antarctic sea ice related to the onset of melt processes do not necessarily translate into changes in snow depth.

4.2.2. Comparison With Previous Studies

Instead of using fixed thresholds for the diurnal brightness temperature variations, as suggested by *Willmes et al*. [2009], our study on surface snowmelt onset retrieval is based on local transition thresholds. Despite this major difference, both studies reveal a comparable latitudinal sequence of snowmelt onsets, from early onset (mid of October) in the marginal ice zone to a later onset (mid January) in the south (Figure 4, section 3.1). On average, our Temporary Snowmelt Onset (TeSMO) is 16 days earlier than the one found by *Willmes et al*. [2009]. The difference is due to fixing the threshold to 10 K, which is significantly higher than the median threshold of 6 K in our study. Thus, *Willmes et al*. [2009] detect surface melt only after several freeze-thaw cycles and significant metamorphism of the snowpack.

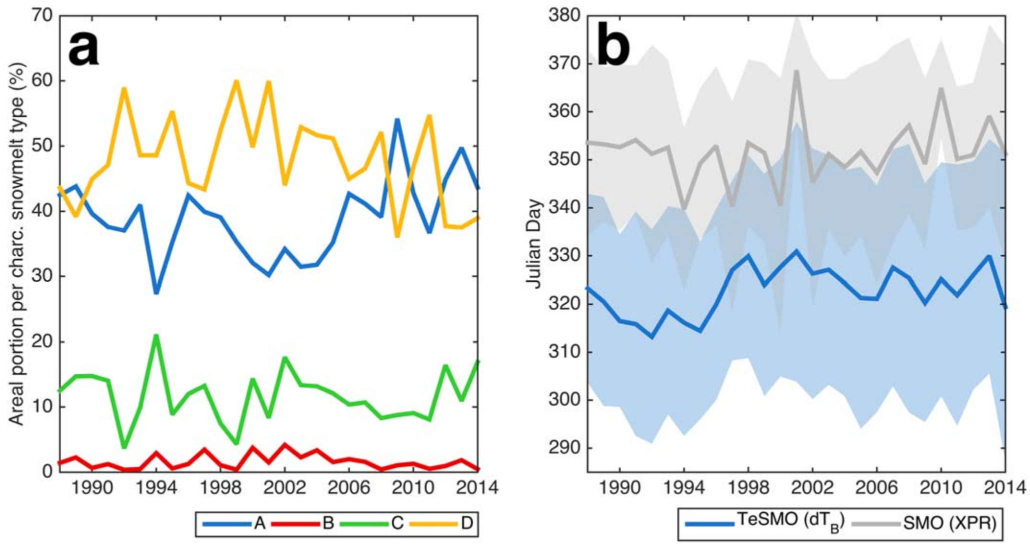

Figure 8. (a) Extent of melt types, as classified in this study (Figure 5, section 3.2): Type A: Diurnal cycles but no continuous melt. Type B: No diurnal cycles but continuous melt. Type C: Diurnal cycles with subsequent continuous melt. Type D: No diurnal cycles and no continuous melt. (b) Dates of Temporary Snowmelt Onset (TeSMO) and Continuous Snowmelt Onset (SMO). Solid lines: Antarctic-wide mean, shaded area: Antarctic-wide standard deviation.

Studies on scatterometer data, e.g., by *Haas* [2001], reveal areas of strong intensities of the backscattered radar signal, associated with the formation of superimposed ice on perennial sea ice. These occur mainly in the northwestern Weddell Sea (67–69°S/51–57°W), in the coastal area of Bellingshausen Sea (e.g., 71.3°S/95.3°W) as well as in the eastern Ross Sea (67.5 to 68.5°S/152 to 157°W). Superimposed ice forms due to enhanced snowmelt and saturation of snow with melt water, but also flooding of sea ice might contribute to superimposed ice formation. Our analysis reveals that diurnal freeze-thaw cycles with subsequent melt in deeper snow layers (Figure 5) prevail for the areas in which the pronounced rise of the backscattering is observed by *Haas* [2001]. Thus, our results support the assumption that in the areas mentioned above, continuous snowmelt causes melt water percolation and formation of superimposed ice.

4.3. Decadal Variability of Snowmelt Patterns

We consider the main advantage of our results in the fact that they provide a large-scale overview on the spatial distribution and frequency of the different types of snow melt onset on Antarctic sea ice. Previous studies of changes in the Antarctic sea-ice area indicate an overall increase in sea-ice extent (SIE) since the late 1970s [*Cavalieri and Parkinson*, 2008; *Stammerjohn et al*., 2012; *Turner et al*., 2015; *Zwally et al*., 2002]. However, one needs to consider regional differences. On average, SIE increased by 3.9% per decade in the Ross Sea whereas a decrease of 3.4% per decade is observed in the Bellingshausen and Amundsen Seas [*Turner et al*., 2015]. These differences are associated with alterations in ice season duration (time period between sea-ice advance and retreat) [*Stammerjohn et al*., 2012]: since 1979/1980, the Ross Sea ice season has lengthened by 25 $\pm$ 4 days whereas the Bellingshausen and Amundsen Sea ice season has decreased by 31 $\pm$ 10 days. Averaged over all Antarctic sea ice, the seasonal sea-ice regime indicates that the ice season is getting longer by up to 20 days per decade.

Figure 8a shows the time series of the spatial extent of the different surface melt types observed from 1988/1989 to 2014/2015, as described above. All four types have no significant trend, but a large interannual variability. The highest range of variation of up to 25% in the areal proportion per snowmelt type is observed for areas with diurnal freeze-thaw cycles but no strong melt (Type A, blue) and areas revealing neither diurnal freeze-thaw cycles at the snow surface nor continuous melt (Type D, yellow).

The temporal evolution of TeSMO and SMO does also show no significant trend (Figure 8b). During the entire period of 27 years, the average TeSMO for the entire Antarctic occurred on 16 November, ranging from 9 November (2009) to 26 November (2001).

Thus, there is no direct link between snowmelt processes and the temporal evolution of sea-ice concentration and extent during the last decades. Instead, variations in weather patterns [*Matear et al*., 2015; *Nghiem et al*., 2016] during spring might well precondition the snow surface and processes in deeper snow layers (e.g., snow metamorphism) leading to an either accelerated or delayed melt progress. Consequently, we see, e.g., in the southern Weddell Sea a clear transition between areas of diurnal freeze-thaw cycles with subsequent continuous melt (Figure 5, Type C, green) in the western part and areas with neither temporary nor continuous melt (Type D, yellow) in the eastern part for most of the time whereas Type D is almost completely absent for 1990/1991, 1996/1997, 2001/2002 and 2010/2011.

5. Conclusions

We developed a new method to detect snowmelt on Antarctic sea ice, which is based on using individual local thresholds applied to the diurnal variation dT_B of the microwave brightness temperatures at 37 GHz (temporary snowmelt onset). We use the cross-polarized ratio (XPR) that combines brightness temperatures at 37 GHz V-polarization and 19 GHz H-polarization to generate a complementary data set of intermittent and continuous melt onset. These melt onset indicators are applied to determine characteristic surface melt patterns on Antarctic sea ice.

Our analysis reveals four surface regimes with substantial differences in their melt characteristics: (Type A) $38.9 \pm 6.0\%$ of all detected melt events are characterized by diurnal freeze-thaw cycles resulting in temporary surface snowmelt but no continuous melt; (Type B) less than 2% reveal continuous melt only; (Type C) $11.7 \pm 4.0\%$ of all events reveal diurnal surface freeze-thaw cycles leading to subsequent continuous strong melt; (Type D) for $47.8 \pm 6.8\%$ no significant temporary or continuous surface melt characteristics are observed at all. Areas characterized by freeze-thaw cycles are more extensive than areas of continuous melt.

The retrieved melt onset dates using per-pixel thresholds consider regional differences in the amplitudes of diurnal freeze-thaw cycles connected to different snow surface properties during the spring-summer transition. With our flexible transition threshold and its modal value of 6 K, compared to the fixed threshold of 10 K by *Willmes et al*. [2006], we enable to detect the first occurrence of temporary surface melt, which might be missed to some extent by the fixed-threshold algorithm. The results of the new algorithm are compared with snow depth data from autonomous monitoring systems (snow buoys) drifting through the Weddell Sea during spring-summer transition 2014/2015. The results show uncertainties in the local point-to-point comparison due to, e.g., local snowdrift events and snow metamorphism, whereas snowmelt processes on a broad-scale (i.e., 100–1000 km) can be descripted by the retrieved melt onset data products.

We apply our algorithm for deriving spatial distributions of the different surface melt types on an SSM/I time series from 1988/1989 to 2014/2015, and determine decadal variabilities in the timing of the melt onsets for freeze-thaw cycles and for continuous snow melt. Previous studies have shown an increasing sea-ice extent, sea-ice concentration, and ice season duration in certain regions of the Antarctic sea ice during the last decades [e.g., *Stammerjohn et al*., 2012, *Turner et al*., 2015], whereas the spatial extent of the four different surface types and the derived melt onset dates do show strong inter-annual variations but no significant trend between 1988/1989 and 2014/2015.

Since diurnal freeze-thaw cycles cause rounding and growth of snow grains [*Willmes et al*., 2009], their onset has a major impact on local optical properties of the snow surface, e.g., albedo and absorption, and thus on the energy budget of Antarctic sea ice. The newly derived continuous snowmelt onset has important implications for the estimation of the sea-ice mass budget. Our analysis indicates that continuous snowmelt takes place often in areas with superimposed-ice formation [*Haas et al*., 2001]. As superimposed ice significantly contributes to the sea-ice mass balance [*Eicken et al*., 1994; *Haas et al*., 2001], our derived data product of the continuous snowmelt onset (types B and C) may be helpful for delimiting positions and extent of superimposed ice formation. The comparison with Snow Buoy data suggests that also continuous melt processes in the perennial snowpack does not necessarily translate into changes in snow depth but might rather affect the internal stratigraphy and density structure of the snowpack.

The presence of liquid water in the snowpack has an impact on sea-ice concentration retrieval [e.g., *Comiso et al*., 1992], and limits snow depth retrieval based on microwave radiometry [*Cavalieri et al*., 2012].

Acknowledgments
SSM/I brightness temperature and sea-ice concentration data were kindly provided by the U.S. National Snow and Ice Data Center (NSIDC, http://nsidc.org), University of Colorado. Autonomous sea-ice measurements from snow buoys were obtained from Meereisportal.de (http://data.seaiceportal.de, grant REKLIM-2012-04). We appreciate the helpful comments of two anonymous reviewers. This work was funded by the Helmholtz Alliance "Remote Sensing and Earth System Dynamics" (HA-310) and the Alfred-Wegener-Institut Helmholtz-Zentrum für Polar- und Meeresforschung.

References

Abdalati, W., and K. Steffen (1995), Passive microwave-derived snow melt regions on the Greenland Ice-Sheet, *Geophys. Res. Lett.*, *22*(7), 787–790.

Abdalati, W., and K. Steffen (1997), Snowmelt on the Greenland ice sheet as derived from passive microwave satellite data, *J. Clim.*, *10*(2), 165–175.

Andersen, S., L. A. Breivik, S. Eastwood, Ø. Godøy, M. Lind, M. Porcires, H. Schyberg (2007), OSI SAF Sea Ice Product Manual, v3. 5, *EUMETSAT OSI SAF, Ocean and Sea Ice Sattelite Application Facility, Tech. Rep. SAF/OSI/met. no/TEC/MA/125*.

Andreas, E. L., and S. F. Ackley (1982), On the differences in ablation seasons of Arctic and Antarctic sea ice, *J. Atmos. Sci.*, *39*(2), 440–447.

Armstrong, R., K. Knowles, M. Brodzik, and M. Hardman (1994), *DMSP SSM/I-SSMIS Pathfinder Daily EASE-Grid Brightness Temperatures. Version 2*, NASA DAAC Natl. Snow and Ice Data Cent. Distrib. Active Arch. Cent., Boulder, Colo.

Arndt, S., and M. Nicolaus (2014), Seasonal cycle and long-term trend of solar energy fluxes through Arctic sea ice, *Cryosphere*, *8*(6), 2219–2233.

Ashcraft, I. S., and D. G. Long (2003), Increasing temporal resolution in greenland ablation estimation using passive and active microwave data, paper presented at Geoscience and Remote Sensing Symposium, IGARSS, IEEE, Toulouse, France.

Belchansky, G. I., D. C. Douglas, and N. G. Platonov (2004), Duration of the Arctic Sea ice melt season: Regional and interannual variability, 1979-2001, *J. Clim.*, *17*(1), 67–80.

Brandt, R. E., and S. G. Warren (1993), Solar-heating rates and temperature profiles in Antarctic snow and ice, *J. Glaciol.*, *39*(131), 99–110.

Brandt, R. E., S. G. Warren, A. P. Worby, and T. C. Grenfell (2005), Surface albedo of the Antarctic sea ice zone, *J. Clim.*, *18*(17), 3606–3622.

Cavalieri, D. J., and C. L. Parkinson (2008), Antarctic sea ice variability and trends, 1979-2006, *J. Geophys. Res.*, *113*, C07004, doi:10.1029/2007JC004564.

Cavalieri, D. J., et al. (2012), A Comparison of snow depth on sea ice retrievals using airborne altimeters and an AMSR-E Simulator, *IEEE Trans. Geosci. Remote Sens.*, *50*(8), 3027–3040.

Comiso, J. C. (1983), Sea ice effective microwave emissivities from satellite passive microwave and infrared observations, *J. Geophys. Res.*, *88*(C12), 7686–7704.

Comiso, J. C., D. J. Cavalieri, C. L. Parkinson, and P. Gloersen (1997), Passive microwave algorithms for sea ice concentration: A comparison of two techniques, *Remote sensing of Environment*, *60*(3), 357–384.

Comiso, J. C., and R. Kwok (1996), Surface and radiative characteristics of the summer Arctic sea ice cover from multisensor satellite observations, *J. Geophys. Res.*, *101*(C12), 28,397–28,416.

Comiso, J. C., and F. Nishio (2008), Trends in the sea ice cover using enhanced and compatible AMSR-E, SSM/I, and SMMR data, *J. Geophys. Res.*, *113*, C02S07, doi:10.1029/2007JC004257.

Comiso, J. C., T. C. Grenfell, M. Lange, A. W. Lohanick, R. K. Moore, and P. Wadhams (1992), Microwave remote sensing of the Southern Ocean ice cover, in *Microwave Remote Sensing of Sea Ice*, edited by F. D. Carsey, pp. 243–259, AGU, Washington, D. C.

Drinkwater, M. R., and X. Liu (2000), Seasonal to interannual variability in Antarctic sea-ice surface melt, *IEEE Trans. Geosci. Remote Sens.*, *38*(4), 1827–1842.

Drobot, S. D., and M. R. Anderson (2001), An improved method for determining snowmelt onset dates over Arctic sea ice using scanning multichannel microwave radiometer and Special Sensor Microwave/Imager data, *J. Geophys. Res.*, *106*(D20), 24,033–24,049.

Eicken, H., M. A. Lange, H. W. Hubberten, and P. Wadhams (1994), Characteristics and distribution patterns of snow and meteoric ice in the Weddell Sea and their contribution to the mass balance of sea ice, *Ann. Geophys.*, *12*(1), 80–93.

Eppler, D. T., L. D. Farmer, A. W. Lohanick, M. R. Anderson, D. J. Cavalieri, J. Comiso, P. Gloersen, C. Garrity, T. C. Grenfell, and M. Hallikainen (1992), Passive microwave signatures of sea ice, in *Microwave Remote Sensing of Sea Ice, Geophys. Monogr. 68*, edited by F. D. Carsey, pp. 47–71, AGU, Washington, D. C.

Flocco, D., D. Schroeder, D. L. Feltham, and E. C. Hunke (2012), Impact of melt ponds on Arctic sea ice simulations from 1990 to 2007, *J. Geophys. Res.*, *117*, C09032, doi:10.1029/2012JC008195.

Foster, J., D. Hall, A. Chang, and A. Rango (1984), An overview of passive microwave snow research and results, *Rev. Geophys.*, *22*(2), 195–208.

Garrity, C. (1992), Characterization of snow on floating ice and case studies of brightness temperature changes during the onset of melt, *Microwave Remote Sens. Sea Ice*, *68*, 313–328.

Gloersen, P., W. J. Campbell, D. J. Cavalieri, J. C. Comiso, C. L. Parkinson, and H. J. Zwally (1992), Arctic and Antarctic sea ice, 1978-1987: Satellite passive-microwave observations and analysis, Special Publication SP-511, 290 pp., NASA, Washington, D. C.

Haas, C. (2001), The seasonal cycle of ERS scatterometer signatures over perennial Antarctic sea ice and associated surface ice properties and processes, *Ann. Glaciol.*, *33*, 69–73.

Haas, C., D. N. Thomas, and J. Bareiss (2001), Surface properties and processes of perennial Antarctic sea ice in summer, *J. Glaciol.*, *47*(159), 613–625.

Hellmer, H. H., C. Haas, G. S. Dieckmann, and M. Schröder (2006), Sea ice feedbacks observed in western Weddell Sea, *Eos Trans. AGU*, *87*(18), 173–179.

Livingstone, C. E., R. Onstott, L. Arsenault, and K. P. Singh (1987), Microwave sea-ice signatures near the onset of melt, *IEEE Trans. Geosci. Remote Sens.*, Ge-25(2), 174–187.

Markus, T., D. J. Cavalieri, A. J. Gasiewski, M. Klein, J. A. Maslanik, D. C. Powell, B. B. Stankov, J. C. Stroeve, and M. Sturm (2006), Microwave signatures of snow on sea ice: Observations, IEEE Transactions on Geoscience and remote Sensing, *44*(11), 3081–3090.

Markus, T., J. C. Stroeve, and J. A. Miller (2009), Recent changes in Arctic sea ice melt onset, freezeup, and melt season length, *J. Geophys. Res.*, *114*, C12024, doi:10.1029/2009JC005436.

Maslanik, J., and J. Stroeve (1999), *Near-Real-Time DMSP SSM/I-SSMIS Daily Polar Gridded Sea Ice Concentrations*, Natl. Snow and Ice Data Cent., Boulder, Colo.[Available at http://nsidc.org/data/docs/daac/nsidc0081_ssmi_nrt_seaice.gd.html.].

Massom, R. A., et al. (2001), Snow on Antarctic Sea ice, *Rev. Geophys.*, *39*(3), 413–445.

Matear, R. J., T. J. O'Kane, J. S. Risbey, and M. Chamberlain (2015), Sources of heterogeneous variability and trends in Antarctic sea-ice, *Nat. Commun.*, *6*, doi:10.1038/ncomms9656.

Mätzler, C., and R. Hüppi (1989), Review of signature studies for microwave remote sensing of snowpacks, *Adv. Space Res.*, *9*(1), 253–265.

Nghiem, S., I. Rigor, P. Clemente-Colón, G. Neumann, and P. Li (2016), Geophysical constraints on the Antarctic sea ice cover, *Remote Sens. Environ.*, *181*, 281–292.

Nicholls, K. W., S. Østerhus, K. Makinson, T. Gammelsrød, and E. Fahrbach (2009), Ice-ocean processes over the continental shelf of the southern Weddell Sea, Antarctica: A review, *Rev. Geophys.*, *47*, RG3003, doi:10.1029/2007RG000250.

Nicolaus, M., C. Haas, J. Bareiss, and S. Willmes (2006), A model study of differences of snow thinning on Arctic and Antarctic first-year sea ice during spring and summer, *Ann. Glaciol.*, *44*, 147–153.

Nicolaus, M., C. Haas, and S. Willmes (2009), Evolution of first-year and second-year snow properties on sea ice in the Weddell Sea during spring-summer transition, *J. Geophys. Res.*, *114*, D17109, doi:10.1029/2008JD011227.

Nicolaus, M., S. Gerland, S. R. Hudson, S. Hanson, J. Haapala, and D. K. Perovich (2010), Seasonality of spectral albedo and transmittance as observed in the Arctic Transpolar Drift in 2007, *J. Geophys. Res.*, *115*, C11011, doi:10.1029/2009JC006074.

Perovich, D. K., and C. Polashenski (2012), Albedo evolution of seasonal Arctic sea ice, *Geophys. Res. Lett.*, *39*, L08501, doi:10.1029/2012GL051432.

Perovich, D. K., T. C. Grenfell, B. Light, and P. V. Hobbs (2002), Seasonal evolution of the albedo of multiyear Arctic sea ice, *J. Geophys. Res.*, *107*(C10), 8044, doi:10.1029/2000JC000438.

Ridler, T., and S. Calvard (1978), Picture thresholding using an iterative selection method, *IEEE Trans. Syst. Man Cybernetics*, *8*(8), 630–632.

Rösel, A., and L. Kaleschke (2012), Exceptional melt pond occurrence in the years 2007 and 2011 on the Arctic sea ice revealed from MODIS satellite data, *J. Geophys. Res.*, *117*, C05018, doi:10.1029/2011JC007869.

Schmitt, C., S. Wassermann, M. Drinkwater, and C. Kottmeier (2004), *Atlas of Antarctic Sea Ice Drift*, Institut für Meteorologoie und Klimaforschung, Universität Karlsruhe, Germany.

Smith, S. D., R. D. Muench, and C. H. Pease (1990), Polynyas and leads: An overview of physical processes and environment, *J. Geophys. Res.*, *95*(C6), 9461–9479.

Stammerjohn, S., R. Massom, D. Rind, and D. Martinson (2012), Regions of rapid sea ice change: An inter-hemispheric seasonal comparison, *Geophys. Res. Lett.*, *39*, L06501, doi:10.1029/2012GL050874.

Tedesco, M. (2015), *Remote Sensing of the Cryosphere*, Wiley Blackwell, Hoboken, doi:10.1002/9781118368909.

Turner, J., J. S. Hosking, T. J. Bracegirdle, G. J. Marshall, and T. Phillips (2015), Recent changes in Antarctic sea ice, *Philos. Trans. R. Soc. A*, *373*(2045), 20140163.

Ulaby, F. T., R. K. Moore, and A. K. Fung (1986), *Microwave Remote Sensing. Active and Passive*. *Vol*. 3. *From Theory to Applications*., pp. 1065–2162, Addison-Wesley, London, U. K.

Webster, M. A., I. G. Rigor, D. K. Perovich, J. A. Richter-Menge, C. M. Polashenski, and B. Light (2015), Seasonal evolution of melt ponds on Arctic sea ice, *J. Geophys. Res. Oceans*, *120*, 5968–5982, doi:10.1002/2015JC011030.

Willmes, S., J. Bareiss, C. Haas, and M. Nicolaus (2006), The importance of diurnal processes for the seasonal cycle of sea-ice microwave brightness temperatures during early summer in the Weddell Sea, Antarctica, *Ann. Glaciol.*, *44*, 297–302.

Willmes, S., C. Haas, M. Nicolaus, and J. Bareiss (2009), Satellite microwave observations of the interannual variability of snowmelt on sea ice in the Southern Ocean, *J. Geophys. Res.*, *114*, C03006, doi:10.1029/2008JC004919.

Willmes, S., M. Nicolaus, and C. Haas (2014), The microwave emissivity variability of snow covered first-year sea ice from late winter to early summer: A model study, *Cryosphere*, *8*(3), 891–904.

Worby, A. P., T. Markus, A. D. Steer, V. I. Lytle, and R. A. Massom (2008), Evaluation of AMSR-E snow depth product over East Antarctic sea ice using in situ measurements and aerial photography, *J. Geophys. Res.*, *113*, C05S94, doi:10.1029/2007JC004181.

Zwally, H. J., J. C. Comiso, C. L. Parkinson, D. J. Cavalieri, and P. Gloersen (2002), Variability of Antarctic sea ice 1979-1998, *J. Geophys. Res.*, *107*(C5), 3041, doi:10.1029/2000JC000733.